

# C<sup>+</sup> distribution around S 1 in $\rho$ Ophiuchi

B. Mookerjea<sup>1</sup>, G. Sandell<sup>2,3</sup>, W. Vacca<sup>3</sup>, E. Chambers<sup>3</sup>, and R. Güsten<sup>4</sup>

<sup>1</sup> Tata Institute of Fundamental Research, Homi Bhabha Road, Mumbai 400005, India e-mail: bhaswati@tifr.res.in

<sup>2</sup> Institute for Astronomy, University of Hawaii, 640 N. Aohoku Place, Hilo, HI 96720, USA

<sup>3</sup> USRA/SOFIA, NASA Ames Research Center, Mail Stop 232-12, Building N232, P.O. Box 1, Moffett Field, CA 94035-0001, USA

<sup>4</sup> Max Planck Institut für Radioastronomie, Auf dem Hügel 69, 53121 Bonn, Germany

latest revision February 16, 2022

## ABSTRACT

We analyze a [C II] 158  $\mu\text{m}$  map obtained with the L2 GREAT receiver on SOFIA of the emission/reflection nebula illuminated by the early B star S 1 in the  $\rho$  Oph A cloud core. This data set has been complemented with maps of CO(3–2), <sup>13</sup>CO(3–2) and C<sup>18</sup>O(3–2), observed as a part of the JCMT Gould Belt Survey, with archival HCO<sup>+</sup>(4–3) JCMT data, as well as with [O I] 63 and 145  $\mu\text{m}$  imaging with *Herschel*/PACS. The [C II] emission is completely dominated by the strong PDR emission from the nebula surrounding S 1 expanding into the dense Oph A molecular cloud west and south of S 1. The [C II] emission is significantly blue shifted relative to the CO spectra and also relative to the systemic velocity, particularly in the northwestern part of the nebula. The [C II] lines are broader towards the center of the S 1 nebula and narrower towards the PDR shell. The [C II] lines are strongly self-absorbed over an extended region in the S 1 PDR. Based on the strength of the [<sup>13</sup>C II] F = 2–1 hyperfine component, [C II] is significantly optically thick over most of the nebula. CO and <sup>13</sup>CO(3–2) spectra are strongly self-absorbed, while C<sup>18</sup>O(3–2) is single peaked and centered in the middle of the self-absorption. We have used a simple two-layer LTE model to characterize the background and foreground cloud contributing to the [C II] emission. From this analysis we estimate the extinction due to the foreground cloud to be  $\sim 9.9$  mag, which is slightly less than the reddening estimated towards S 1. Since some of the hot gas in the PDR is not traced by low J CO emission, this result appears quite plausible. Using a plane parallel PDR model with the observed [O I](145)/[C II] brightness ratio and an estimated FUV intensity of 3100–5000 G<sub>0</sub> suggests that the density of the [C II] emitting gas is  $\sim 3 - 4 \times 10^3 \text{ cm}^{-3}$ .

**Key words.** ISM: Clouds – Submillimeter: ISM – ISM: lines and bands – ISM: individual ( $\rho$  Oph A) – ISM: molecules – H II regions

## 1. Introduction

Photon Dominated Regions (PDRs) are regions where FUV ( $6 \text{ eV} < h\nu < 13.6 \text{ eV}$ ) radiation from young massive stars dominate the physics and the chemistry of the interstellar medium (Tielens & Hollenbach 1985). The PDRs play an important role in reprocessing much of the energy from stars and re-emitting this energy in the infrared-millimeter wavelengths. Most of the mass of the gas and dust in the Galaxy resides in PDRs (Hollenbach & Tielens 1999). In the far infrared the most important cooling lines are the fine structure lines of [C II] at 158  $\mu\text{m}$ , and [O I] at 63 & 145  $\mu\text{m}$  and to a lesser extent high-*J* CO lines, while PAH emission and H<sub>2</sub> lines dominate in the near- and mid-IR.

The  $\rho$  Ophiuchi dark cloud complex is the nearest low- and intermediate-mass star forming region (see Wilking, Cagné & Allen (2008) for a recent review). The mean distance to  $\rho$  Oph is  $137.3 \pm 1.2$  pc based on trigonometric parallax observations with the Very Long Baseline Array (VLBA), while the eastern streamer appears to be  $\sim 10$  pc further away (Ortiz-León et al. 2017). The most massive cores in  $\rho$  Oph dark cloud complex are  $\rho$  Oph A (Loren, Wootten, & Wilking 1990) in L1688 and L1689N, each of which is connected with a filamentary system of streamers extending to the north-east over tens of parsecs (e.g., Loren 1989). While only little star formation activity is observed in the streamers, the westernmost core,  $\rho$  Oph A, harbors a rich cluster of young stellar objects (YSOs) ranging from young Class 0 protostars to more evolved Class III objects and is distinguished by a high star-formation efficiency.

Yui et al. (1993) did an extended [C II] map with 15' spatial resolution of the  $\rho$  Ophiuchi dark cloud using the balloon-borne telescope BICE. They found extended [C II] emission throughout the cloud (8 pc  $\times$  6 pc) with the peak emission centered on the highly reddened B2 V star HD 147889 with perhaps minor contributions from the embedded B stars S 1 and SR 3.

Recently Larsson & Liseau (2017) have studied the  $\rho$  Oph A region with HIFI and PACS on the *Herschel Space Observatory* together with archival *ISO* ISOCAM-CVF data. Their spectrophotometric ISOCAM observations of pure rotational lines of H<sub>2</sub> and polycyclic aromatic hydrocarbon (PAH) molecules outline a clear spherical shell structure of warm PDR gas around the embedded star S 1 with a radius of  $\sim 80''$ . The observations of the [O I] lines at 63 and 145  $\mu\text{m}$  using PACS show that not only do the [O I] lines mark the boundary seen in H<sub>2</sub>, but also show significant emission throughout the region around the exciting star S 1. The map of the line flux ratio  $F_{63 \mu\text{m}}/F_{145 \mu\text{m}}$  shows remarkably low values in some regions, which suggests the presence of a cold foreground cloud that absorbs most of the <sup>3</sup>P<sub>1</sub>–<sup>3</sup>P<sub>2</sub> 63  $\mu\text{m}$  radiation but leaves the higher level <sup>3</sup>P<sub>0</sub>–<sup>3</sup>P<sub>1</sub> 145  $\mu\text{m}$  line unaffected. All the existing observations of the PDR tracers of the S 1 PDR unfortunately lack velocity information, hence the interplay between the cold foreground cloud and the warmer background PDR material is still unexplored.

In this paper we present velocity resolved [C II] maps of an area around the S 1 PDR in  $\rho$  Oph A. Here we aim to study the emission from the S 1 PDR to (a) understand the impact of the PDR if any on the molecular cloud to the west and (b) detect and characterize the foreground absorbing cloud observed in [O I].

## 2. Datasets

### 2.1. SOFIA

We have retrieved observations of the  $^2P_{3/2} \rightarrow ^2P_{1/2}$  fine structure transition of ionized carbon ( $C^+$ ) at 1900.5369 GHz ( $157.74 \mu\text{m}$ ) and the  $^3P_1 \rightarrow ^3P_0$  [N II] line at 1461.1338 GHz ( $205 \mu\text{m}$ ), of  $\rho$  Oph A from the data archive of the Stratospheric Observatory for Infrared Astronomy (SOFIA Young et al. 2012). The observations (PI: Di Li) were done using the German REceiver for Astronomy at Terahertz frequencies (GREAT; Heyminck et al. 2012) on July 16 and 20, 2011. The beam size for [C II] was  $15''.3$  and the velocity resolution before smoothing was  $0.029 \text{ km s}^{-1}$ , while the beamsize for [N II] was  $21''$ . The [C II] map extends over a  $220'' \times 200''$  area and was done in total power on-the-fly mode. The map was divided into five sub-maps, each scanned in Dec, and sampled every  $8''$ , with a step size between scans of  $8''$ . The map was centered on  $(\alpha, \delta) = (16^{\text{h}} 26^{\text{m}} 27^{\text{s}}.60, -24^{\circ} 23' 56''.3)$  (J2000) using an off-position at  $16^{\text{h}} 29^{\text{m}} 49^{\text{s}}.0, -24^{\circ} 29' 31''.0$  (J2000). We used a main beam efficiency of 0.51 and 0.54 (Heyminck et al. 2012) to convert the observed antenna temperatures to main beam brightness temperature ( $T_{\text{mb}}$ ) for [C II] and [N II], respectively. [N II] was not detected anywhere in the map.

Finally we retrieved fully processed level 3 SOFIA/FORCAST images at 11.1, 19.7, 31.5, and  $37.1 \mu\text{m}$  (Herter et al. 2012). These were taken in dichroic mode on 2014-03-29 covering the S1 field (Program ID: 02\_0070/Lee Mundy). For a description of the FORCAST data reduction pipeline, see Herter et al. (2013).

### 2.2. JCMT Gould Belt Survey and ISOCAM data

For comparison with the [C II] data, we have used maps of the  $J=3-2$  transition of CO,  $^{13}\text{CO}$  and  $C^{18}\text{O}$  (White et al. 2015) and  $J=4-3$  transition of  $\text{HCO}^+$ . The CO (and its isotopes) datacubes were kindly provided to us by Dr. Emily Daubrek-Maunder. The observations were taken using the Heterodyne Array Receiver Program (HARP) (Buckle et al. 2009) on the James Clerk Maxwell Telescope (JCMT)<sup>1</sup>, Hawaii. The  $C^{18}\text{O}$ ,  $^{13}\text{CO}$  and CO  $J=3-2$  rest frequencies are 329.330525, 330.5879601 and 345.7959899 GHz, respectively. HARP has a beamsize of  $14''$  at 345 GHz. The CO(3-2) data have a spectral resolution of  $1 \text{ km s}^{-1}$ , while the  $C^{18}\text{O}$  and  $^{13}\text{CO}$  data have a resolution of  $0.1 \text{ km s}^{-1}$ . The  $\text{HCO}^+(4-3)$  data set, corresponding to the proposal M11AU13, was downloaded directly from the JCMT archive at the Canadian Astronomical Data Centre (CADC).

We have also retrieved fully processed ISOCAM image cubes (CAM1 & CAM4) including pipeline processed photometry of S1 from the ISO Data Archive (Lorente 2006).

<sup>1</sup> The James Clerk Maxwell Telescope is operated by the East Asian Observatory on behalf of The National Astronomical Observatory of Japan; Academia Sinica Institute of Astronomy and Astrophysics; the Korea Astronomy and Space Science Institute; the Operation, Maintenance and Upgrading Fund for Astronomical Telescopes and Facility Instruments, budgeted from the Ministry of Finance (MOF) of China and administrated by the Chinese Academy of Sciences (CAS), as well as the National Key R&D Program of China (No. 2017YFA0402700). Additional funding support is provided by the Science and Technology Facilities Council of the United Kingdom and participating universities in the United Kingdom and Canada.

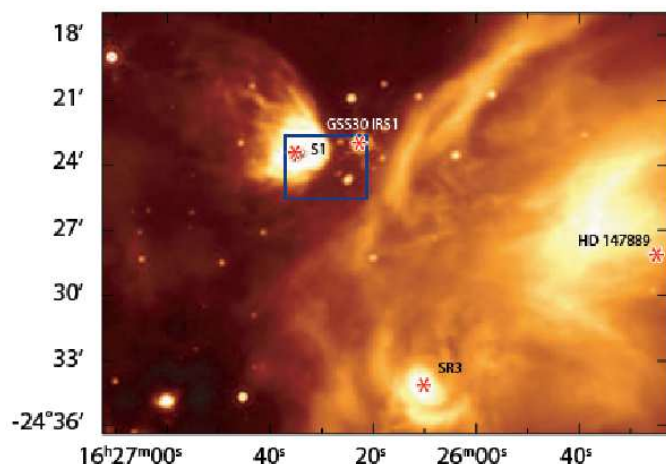


**Fig. 1.** Part of MIPS  $24 \mu\text{m}$  image extracted from Fig. 3 in Padgett et al. (2008). The image shows the four main FUV sources in the northern part of  $\rho$  Oph: S1, GSS 30 IRS1, SR3 and HD 147889, which are labeled and marked with red symbols. The blue rectangle shows the area mapped in [C II] with GREAT.

## 3. FUV sources in the $\rho$ Oph A cloud

The  $\rho$  Oph A cloud core is between the large reflection nebula illuminated by the B2 V star HD 147889 on the western side and the H II region illuminated by the early B star S1 on the eastern side with the embedded B9 - A0 V star SR3 (Lada & Wilking 1984) to the south, (see Fig. 1). In the  $\rho$  Oph A core region there is another bright star  $\sim 175''$  west of S1. This bright mid-IR source is GSS 30 IRS1 (2MASS J16262138-2423040), a low mass Class I source illuminating a small bipolar reflection nebula (Weintraub et al. 1993). In the mm/sub-mm  $\rho$  Oph A stands out as a north-south ridge of several bright dust condensations curving to the southeast at the southern end (André, Ward-Thompson & Barsony 1993; Motte et al. 1998; Liseau et al. 2015). One of these sub-mm sources is VLA 1623, the prototypical Class 0 source (André, Ward-Thompson & Barsony 1993), which drives a large, highly collimated jet in the NW-SE direction.

**S1:** S1 is an embedded early B star in the  $\rho$  Oph A cloud at a distance of  $138 \pm 1.7 \text{ pc}$  (Ortiz-León et al. 2017). It is the brightest near-IR source in  $\rho$  Ophiuchus (Grasdalen, Strom, & Strom 1973) and a strong X-ray source (Montmerle et al. 1983). It was first detected as a radio source in  $\rho$  Oph by Brown & Zuckerman (1975) (BZ #4), who suggested that it was a compact H II region ionized by a B3 star. A detailed VLA study by André et al. (1988) at 5 and 15 GHz in the C/D hybrid configuration showed that the radio emission originates from a nonthermal unresolved core surrounded by a thermal extended halo. They inferred that the compact nonthermal emission is gyrosynchrotron emission from an extended magnetosphere around the star, while the halo is free-free emission from an optically thin H II region. From the observed free-free emission, 4 mJy, at 5 GHz, and a half power radius of  $\sim 10''$ , they derived a spectral type of B3.5 (ZAMS) with an effective temperature of  $T_{\text{eff}} = 17,000 \text{ K}$ . The multi-epoch VLBI trigonometric parallax study (Ortiz-León et al. 2017) resolves S1 into a binary with a separation of  $\sim 20 - 30 \text{ mas}$  consistent with near-IR lunar occultations by Richichi et al. (1994); Simon et al. (1995), who found S1 to have a late type secondary with a projected distance of 20 mas. From an orbit analysis of the VLBA data Ortiz-León et al. (2017) derive a mass of  $5.8 M_{\odot}$  for the primary and  $1.2 M_{\odot}$  for

the secondary. These mass estimates correspond roughly to B4V and F5V spectral types.

S 1 is too faint in the optical ( $V = 16.5$  mag) to allow accurate spectral classification. Cohen & Kuhi (1979) did not detect H $\alpha$  at all and assigned it a spectral class of B2. Later, based on the equivalent width of the H $\alpha$  line, Bouvier & Appenzeller (1992) classified it as a B4 star, while Wilking et al. (2005) suggested a spectral type of B3. The star is very bright in the near-IR and barely visible in the mid-IR, where the emission is completely dominated by the surrounding reflection nebula, which saturates the MIPS image close to S 1, see Fig. 1. It was not detected in any of the WISE bands. Lada & Wilking (1984) used ground based near and mid-IR photometry to determine the bolometric luminosity of S 1. They found no IR excess for the star after dereddening the observed flux densities with 12 mag of visual extinction. By fitting a blackbody curve to the extinction corrected spectral energy distribution they derived an effective temperature,  $T_{eff} = 16000$  K, and a luminosity,  $L = 1100 L_{\odot}$  (corrected for a distance of 140 pc).

Using the VizieR photometry viewer, we have compiled all available photometric measurements (with uncertainties) of S 1. The measurements include values in the Johnson optical (B band) and near-infrared (JHK) filters, POSS filters (J, F, i), Gaia G band filter, PanStarrs optical (g, r, i) filters, SDSS optical ( $i'$ ) filter, Elias near-infrared (J, H, K, L') filters, 2MASS near-infrared (J, H, K<sub>s</sub>) filters, IRAC infrared (3.6, 4.5, 5.8, and 8.0  $\mu$ m) filters, NICMOS near-infrared (1.10 and 1.60  $\mu$ m) filters, ISOCAM (CAM1: 3.0, 3.3, and 3.7  $\mu$ m; CAM4: 5.0 - 5.7  $\mu$ m). Analysis of the FORCAST images show that S 1 is undetected in all filters. The 3- $\sigma$  upper limit at 11.1  $\mu$ m is 180 mJy. We then attempted to fit the resulting spectral energy distribution with a blackbody function with reddening. We adopted the Rieke & Lebofsky (1985); Rieke, Rieke & Paul (1989) extinction curve. A straightforward fit to the data, for a fixed distance of 138 pc, but without constraints on the reddening, radius, or temperature, does not yield results that are consistent with either main sequence stellar parameters or previous determinations of the extinction or spectral type for S 1.

Because the reddening appears to be so large, the photometric data provide relatively little power to constrain the stellar temperature. Therefore we fixed the temperature at 17000 K, corresponding to that for a B4V star. For consistency, we also fixed the radius to be that appropriate for a B4V star (4.35  $R_{\odot}$ ; Schmidt-Kaler 1982). This leaves the reddening,  $E_{B-V}$ , as a free parameter. While a total optical reddening value of  $A_V \sim 12$  mag, consistent with previous determinations, then provides a reasonable fit to the optical data, we find that the model overestimates the photometric observations in the near-infrared. In fact, we find that no value of the reddening with the standard extinction law yields a model that can adequately fit all of the photometric data. Various authors have claimed that the reddening law towards the Ophiuchus cloud is non-standard, with values of  $R_V$  as high as 4.2 reported (Chini 1981; Andersson & Potter 2007; Lee et al. 2018). Therefore we allowed the  $R_V$  value to vary along with the  $E_{B-V}$  value. With the adopted stellar parameters, we find that  $E_{B-V} \sim 3.8$  and  $R_V \sim 3.35$  provides a good representation of all the photometric data points from the optical out to 10  $\mu$ m, and is consistent with our measured upper limit at 11.1  $\mu$ m (see Fig. 2). These values correspond to a total extinction in the optical of  $A_V = 12.7$  mag. A slightly larger value of the total reddening ( $A_V = 13.3$ ) is required to fit the data if an earlier spectral type (B3V) is adopted, but again a non-standard  $R_V$  value of 3.4 is necessary. Both of these  $R_V$  values are consistent with the angular variations in  $R_V$

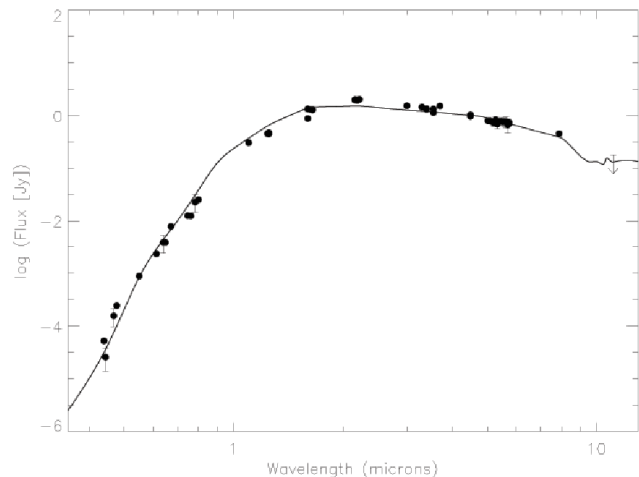


**Fig. 2.** Spectral Energy Distribution (SED) for S 1 based on all existing photometry. The solid curve represents the SED for a reddened blackbody corresponding to a B4V star ( $T_{eff} = 17000$  K,  $R = 4.35 R_{\odot}$ ) with an  $E_{B-V} = 3.8$  and  $R_V = 3.35$  (that is,  $A_V = 12.7$  mag), see Section 3.

found by Lee et al. (2018) for the  $\rho$  Oph cloud complex.

**GSS 30 IRS 1:** This is a deeply embedded low-mass Class I protostar, which illuminates a bipolar reflection nebula and drives a molecular outflow. Je et al. (2015) did a full range scan of GSS 30 IRS 1 with *Herschel*/PACS and found extended emission in both [O I] and [C II]. The [O I] emission is most likely shock excited, while the [C II] emission is PDR emission from the reflection nebula. Je et al. (2015) estimate the far-ultraviolet radiation field is in the range 3 to 20  $G_0$ , where  $G_0$  is in units of the Habing field, defined as  $G_0 = 1.6 \times 10^{-3} \text{ erg cm}^{-2} \text{ s}^{-1}$  (Habing 1968).

### 3.1. S 1 PDR

S 1 has created a large cigar shaped “cavity”, which may extend as far as  $\sim 550''$  to the east northeast, and  $\sim 80''$  to the west southwest, where the expansion is blocked by the dense surrounding molecular cloud, see Fig. 1. The projected major axis of the reflection/emission nebula is therefore  $\sim 0.6$  pc. The morphology of the S 1 reflection nebula resembles NGC 2023 (Sandell et al. 2015), i.e., both show ellipsoidal cavities, which interact strongly with the surrounding dense molecular cloud and expand more freely to the opposite side of the nebula, where the density of the surrounding cloud is much lower. As found in NGC 2023 we see filaments and lumpy ridges in the IRAC images, where the S 1 reflection nebula expands into the dense molecular cloud, suggesting that the dense surrounding cloud is clumpy. There is a bright ridge  $\sim 20''$  south of S 1, which dominates the emission in the mid-IR. The [C II] emission in our map is completely dominated by the reflection nebula illuminated by S 1, although there may be some marginal contribution from GSS 30. The same is true for [O I], even though one can also see faint [O I] emission from shock excited [O I] in the VLA 1623 outflow and even stronger emission from GSS 30. (Larsson & Liseau 2017; Nisini et al. 2015; Je et al. 2015).

## 4. Results

Figure 3 shows comparison of measured [C II] intensity distribution integrated over the velocity interval 0–10 km s<sup>-1</sup> with emission from other PDR tracers (8 μm dust continuum and [O I] at 63 μm) and from molecular material at moderate (CO(3–2) and its isotopes) and high densities (HCO<sup>+</sup>(4–3)). The emission distribution of the PDR tracers is markedly different from the molecular gas tracers. Among the molecular gas tracers the CO(3–2) emission is detected over the whole area and does not seem to trace the PDR emission at all. The strongest CO emission comes from the blue outflow lobe powered by the Class 0 source VLA 1623. There is strong HCO<sup>+</sup>(4–3) emission from the dense cores in the ρ Oph A ridge. Additionally, HCO<sup>+</sup> outlines the dense compressed gas layer to the west and south, where the PDR shell is expanding into the dense molecular cloud. The [C II] emission is completely dominated by the strong PDR emission from the emission/reflection nebula surrounding S 1 with only faint emission west of the S 1 PDR. This faint [C II] emission is probably mostly from the surface layers of the molecular cloud, possibly enhanced by FUV radiation from GSS 30 IRS 1. The 8 μm emission, which is dominated by PDR emission is strikingly similar to [C II], [C II] and 8 μm emission both peak west and south of S 1. The [O I] emission is also dominated by the S 1 PDR similar to [C II]. However, [O I] also clearly shows shock excited emission from the bipolar outflows powered by VLA 1623 and GSS 30, where the [C II] emission is faint or completely absent. Additionally [O I] shows a spur (protrusion) of emission sticking out of the PDR shell approximately straight west from S 1. This feature appears to be real, since it is also seen in the [O I] map analyzed by Nisini et al. (2015). It is not evident in the integrated [C II] image, although there is a hint of it in the [C II] channel maps (Fig 3) at +2 km s<sup>-1</sup>. In the H<sub>2</sub> emission observed with ISOCAM-CVF (Larsson & Liseau 2017) the hot PDR shell is completely dominating, but especially in the S2 line we can also see additional H<sub>2</sub> emission inside the PDR region, particularly in the southwestern part of the PDR.

Figure 4 presents channel maps of 1 km s<sup>-1</sup> wide velocity bins ranging from -1 km s<sup>-1</sup> to 6 km s<sup>-1</sup>. The maps clearly show the two main velocity peaks, the first between 0–3 km s<sup>-1</sup> and the second 5–6 km s<sup>-1</sup>. Comparison of the [C II] channel maps with the CO (and its isotopologues) channels show that the higher velocity component is detected only in CO(3–2) and not in the rarer isotopologues (Fig. B.1, B.2, B.3). HCO<sup>+</sup>(4–3) is our only high density tracer,  $n_{crit} = 2 - 3 \times 10^6$  cm<sup>-3</sup> (Shirley 2015), and the only line, perhaps with the exception of C<sup>18</sup>O, which is unaffected by self-absorption. The upper energy level,  $E_u/k = 42.8$  K, however, is rather low. Therefore the emission is dominated by the dense cold cores in the ρ Oph A cloud, which is seen both in the integrated intensity map (Fig.3) as well as in the channel maps (Fig. B.4).

The position-velocity diagrams derived for cuts at position angles of -135° and -45° show that the [C II] lines are broader towards the center of the S 1 nebula and narrower towards the PDR shell (Fig. 5). This suggests that the [C II] emission has contribution from the entire C II region as well as the front and back of the PDR shell. The [C II] emission is dominantly blue-shifted relative to the systemic velocity, indicating that the emission is dominated by photo evaporation flows from the dense PDR shell. Such emission would be blue-shifted if the densest PDR region is behind the star, i.e. the reflection nebula is inclined towards the line of sight, so that the large extended lobe northeast of the star is largely coming towards us. Unfortunately our [C II] map does not cover the eastern part of the nebula. Therefore we can-

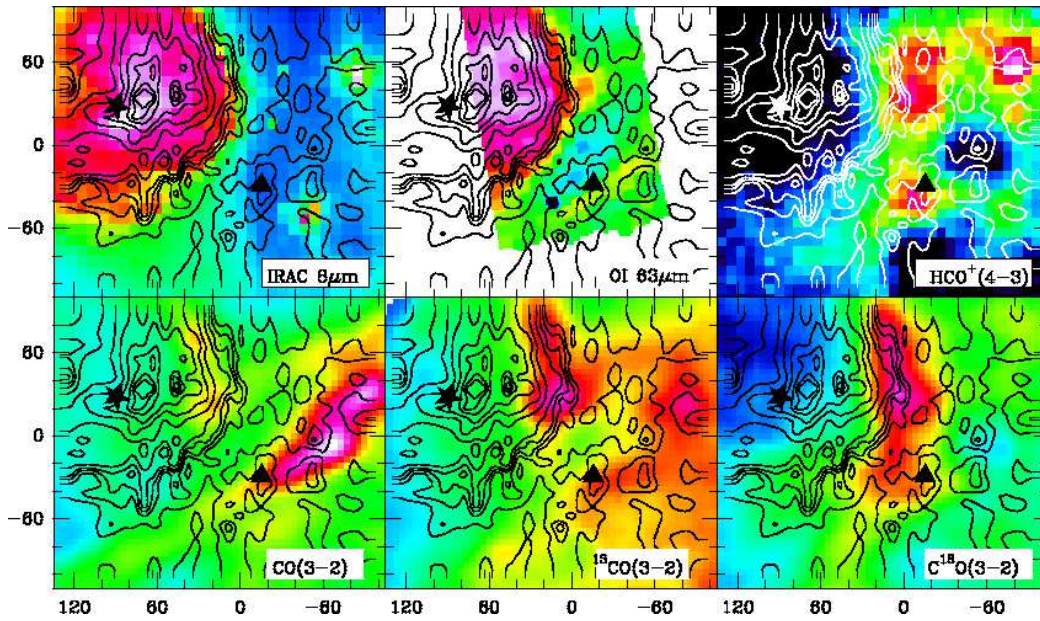
not confirm the proposed geometry of the reflection nebula from the existing data sets.

Figure 6 show the [C II] spectrum averaged over the two regions shown in Fig. 4, compared with the average spectra of CO and its isotopes over the same region. We find that in Box 1, located to the north, only CO(3–2) and [C II] show double peaked spectra, while there is a hint of a shoulder in <sup>13</sup>CO(3–2). C<sup>18</sup>O(3–2) shows a single-peaked spectrum. The strongest hyperfine component of [<sup>13</sup>C II], i.e. F = 2–1, red-shifted by 11.2 km s<sup>-1</sup>, is also detected with a peak temperature of ~ 8.5 K, suggesting that the [C II] emission is optically thick in most of the region. A Gaussian fit of the [<sup>13</sup>C II] component gives a  $v_{LSR} = 3.1$  km s<sup>-1</sup> (relative to the rest frequency of the F = 2–1 line). We get exactly the same velocity for C<sup>18</sup>O, confirming that both CO and [C II] are strongly self-absorbed. The ratio of the integrated intensities of [C II] and <sup>13</sup>[C II] F = 2–1 is ~ 27. The intensity of the F = 2–1 transition of [<sup>13</sup>C II] is 0.625 of the total [<sup>13</sup>C II] intensity. Thus, the ratio of intensities of [C II] to [<sup>13</sup>C II] is ~ 17, which corresponds to an optical depth of 3.7 for [C II]. Further based on the two-component LTE model (Table 1) for the emission (background) component we had derived  $N(C^+) = 5.6 \times 10^{18}$  cm<sup>-2</sup>. This  $N(C^+)$  corresponds to an optical depths of 1.6 and 6, for temperatures of 300 K (typical PDR temperature) and 80 K ( $T_{ex}$  derived from the LTE analysis) respectively. This confirms that [C II] is optically thick and it is not possible to discern any depletion of <sup>13</sup>C<sup>+</sup> due to fractionation. For Box 2, which is south of S 1, the self-absorption, is even more striking and seen in <sup>13</sup>CO as well. Here there is only a hint of the [<sup>13</sup>C II] F = 2–1 hyperfine component, because some of the spectra had rather poor baselines. However, as in Box 1, C<sup>18</sup>O peaks in the middle of the self-absorption confirming that double peaked spectra are caused by self-absorption from cold foreground gas. We discuss the foreground absorption in more detail in Sec. 5.

## 5. The self-absorbing C<sup>+</sup> cloud

The available velocity resolution of the [C II] data has enabled the detection of strongly self-absorbed spectral profiles over an extended region in the S 1 PDR of ρ Oph A. This absorption dip is consistent with the results of spectrally unresolved observations of the two fine-structure transitions of [O I] at 63 and 145 μm, which had also suggested the presence of a foreground absorbing cloud. Here, we take advantage of the available velocity information and characterize the background and foreground cloud using a two-layer Local Thermodynamic Equilibrium (LTE) model. We used the CASSIS<sup>2</sup> software (Vastel et al. 2015), to model the average spectral profiles of [C II], <sup>13</sup>CO(3–2) and C<sup>18</sup>O(3–2) assuming a warm background and a colder foreground component (Fig. 7). CASSIS allows a combined fit of the two components to the observed spectrum of a species with the following adjustable parameters: column density ( $N$ ), excitation temperature ( $T_{ex}$ ),  $v_{LSR}$ , FWHM of the line ( $\Delta v$ ) and size of the source ( $\theta$ ). We have assumed both components to be Gaussians. The results of the fit are presented in Table 1. We find that the relative abundance of the C<sup>18</sup>O and <sup>13</sup>CO molecules in the two components are significantly different. For the warmer component the ratio is ~ 8.8, while it is ~ 14 for the colder component, showing that <sup>13</sup>CO is significantly optically thick both in the foreground and the background cloud. We can convert the derived C<sup>18</sup>O column densities (Table 1) to total column densities using the empirical relationship derived by Frerking, Langer & Wilson (1982) for ρ Oph:

<sup>2</sup> <http://cassis.irap.omp.eu>



**Fig. 3.** Contours of integrated (0–10 km s<sup>-1</sup>) [C II] intensity map of ρ Oph A compared with color images of (Top, left) IRAC 8 micron, (Top, middle) PACS [O I] 63 μm, (Top, Right) JCMT HCO<sup>+</sup>(4–3), (Bottom, Left) CO(3–2), (Bottom, Middle) <sup>13</sup>CO(3–2) and (Bottom, Right) C<sup>18</sup>O(3–2). The [C II] contours are at 25, 40, 50, 60, 75, 100, 120, 140, 160, 170, 175 and 180 K km s<sup>-1</sup>. The filled star and triangle respectively, denote the positions of the star S 1 and the young stellar object VLA 1623.

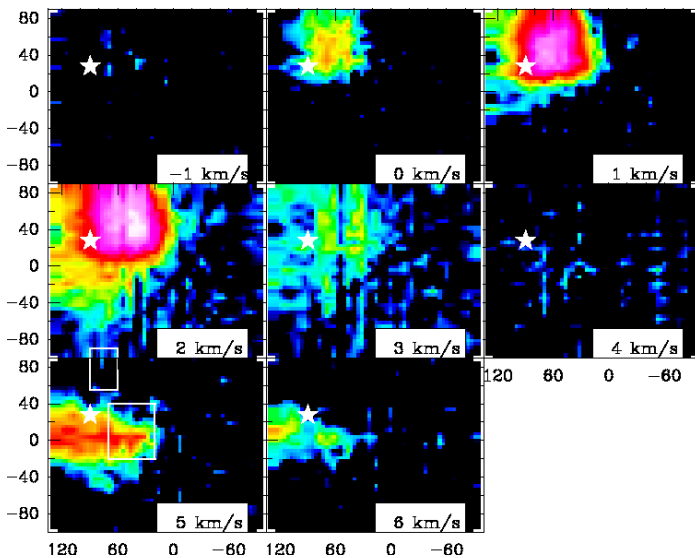


**Fig. 4.** [C II] channel maps of 1 km s<sup>-1</sup> wide velocity channels spaced by 1 km s<sup>-1</sup>. The color scale ranges from 5 to 70 K km s<sup>-1</sup>.

$$N(H_2) = \left[ \frac{C^{18}O}{1.7 \times 10^{14}} + 3.9 \right] \times 10^{21} \text{ cm}^{-2}$$

which gives us  $9.3 \times 10^{21} \text{ cm}^{-2}$  and  $5.6 \times 10^{22} \text{ cm}^{-2}$  for the foreground and background cloud, respectively. If we take the derived foreground column density and transform it to visual extinction assuming normal gas to dust ratio, i.e.,  $N(H_2)/A_V = 0.94 \times 10^{21} \text{ molecules cm}^{-2} \text{ mag}^{-1}$  (Bohlin et al. 1978; Frerking, Langer & Wilson 1982), we get an extinction of 9.9 mag. This is lower than the estimated reddening towards S 1,  $A_V = 12.7 \text{ mag}$ , see Sect. 3. This is to be expected, since C<sup>18</sup>O does not trace the hot gas in the PDR. We can get a rough estimate for the column density of the gas in the PDR by using the de-

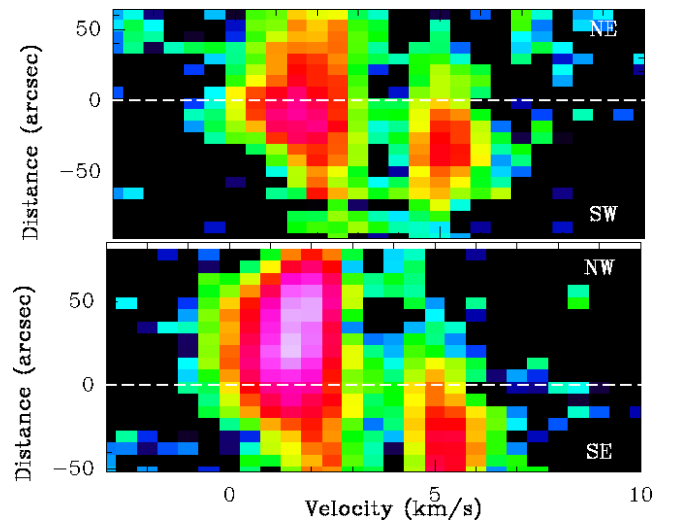


**Fig. 5.** [C II] position-velocity diagrams at position angles of -135° (Top) and -45° (Bottom). The position of S 1 marked with the dotted line.

rived  $N(C^+)$  for the foreground [C II] (Table 1). If we assume that most of the carbon is ionized, i.e.  $[C/H] = 10^{-4}$ , we get  $N(H_2) = 5.3 \times 10^{21} \text{ cm}^{-2}$ , or 5.6 mag. This is almost certainly an overestimate, since some of the carbon is likely to be neutral or tied up in molecules like CO.

## 6. Discussion

[C II] and [O I] are some of the best tracers of PDRs (Hollenbach & Tielens 1999), since they cover a large range of physical condition present in many PDRs. The [C II] 158 μm line, assumed to be largely optically thin, can be used to determine the total mass of the emitting gas. However, with the advent of the high spectral resolution spectrometers like Herschel/HIFI and SOFIA/GREAT there has been a paradigm shift

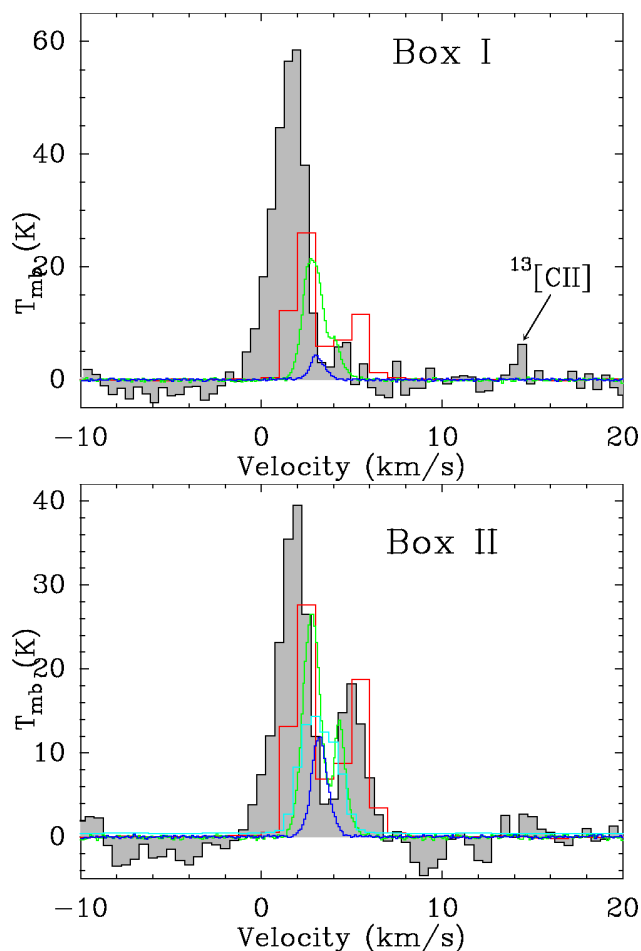


**Fig. 6.** Average spectra of [C II] (black), CO(3–2) (red),  $^{13}\text{CO}(3-2)$  (green) and  $\text{C}^{18}\text{O}(3-2)$  (blue) over the regions I and II marked in Fig. 4.

**Table 1.** Results of fitting of two-component LTE models to average spectra corresponding to the double-peaked profiles

Species	$v_{\text{LSR}}$	$\Delta v$	$T_{\text{ex}}$	$N$	$\theta$
	$\text{km s}^{-1}$	$\text{km s}^{-1}$	K	$\text{cm}^{-2}$	''
$\text{C}^+$	$3.1 \pm 0.1$	$2.7 \pm 0.2$	$80.8 \pm 7.0$	$(5.6 \pm 2.3) 10^{18}$	50
	$3.7 \pm 0.1$	$1.6 \pm 0.1$	$10.5 \pm 0.3$	$(5.3 \pm 0.8) 10^{17}$	30
$^{13}\text{CO}$	$3.4 \pm 0.1$	$1.5 \pm 0.1$	$66.3 \pm 10.5$	$(7.5 \pm 0.1) 10^{16}$	$43 \pm 5$
	$3.7 \pm 0.1$	$0.9 \pm 0.1$	$6.8 \pm 1.3$	$(1.3 \pm 0.1) 10^{16}$	$31.2 \pm 2.1$
$\text{C}^{18}\text{O}$	$3.3 \pm 0.1$	$1.1 \pm 0.1$	70	$(8.9 \pm 0.5) 10^{15}$	50
	$3.6 \pm 0.1$	$0.8 \pm 0.1$	12	$(9.2 \pm 3.3) 10^{14}$	$30.1 \pm 0.1$

in our understanding of the abundance and ubiquity of  $\text{C}^+$ . Not only was the [C II] line found to be optically thick, a fact often clearly substantiated by the detection of hyperfine lines of  $^{13}\text{C}^+$  (Ossenkopf et al. 2013), but a significant fraction of  $\text{C}^+$  emission was found to arise from the ISM where no corresponding CO emission was detected in both our Galaxy (GOTC+ Langer et al. 2010) and external galaxies (Mookerjea et al. 2016).

Our [C II] observations of  $\rho$  Oph-A with SOFIA/GREAT has also provided useful insight into the distribution of the PDR material, particularly in the region around the B-type star S 1. Unlike the emission from CO (and its isotopes) and to some extent [O I] the [C II] emission is completely dominated by the emission/reflection nebula illuminated by S 1. This suggests that the observed [C II] emission is primarily due to the FUV radiation from S 1 with a negligible contribution from HD 17889. The

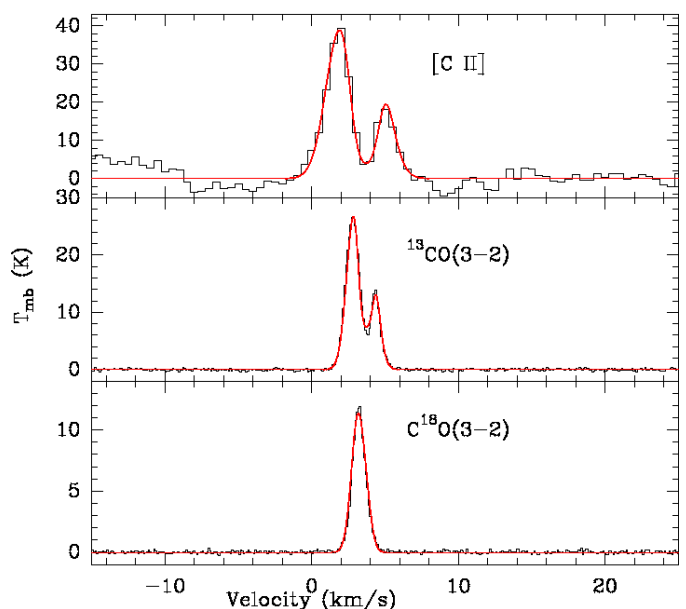


**Fig. 7.** Two component LTE model fits (in red) to average spectra obtained using CASSIS. The fitted parameters are presented in Table 1.

PDR is a slightly asymmetric sphere which is pressure-bound to the south and west due to the enhanced density of the dense  $\rho$  Oph-A molecular cloud and has an average radius of  $80''$ . It almost certainly extends much further to the northeast (see Fig. 1), where the [C II] emission has not yet been observed.

Because we only have velocity resolved  $\text{C}^+$  spectra of the PDR emitted region, the two-component (emission and absorption) model fitted to the [C II] emission is not well constrained. There is a possible degeneracy between the column density of  $\text{C}^+$  and the size of the emission region. Our current model shows consistent excitation temperatures and sizes for [C II] and the CO lines, although owing to the complication of the presence of the foreground absorption, the intrinsic [C II] emission is not well constrained. Graf et al. (2012) detected similar optically thick [C II] lines affected by strong self-absorption in NGC 2024 and estimated a very high value of  $N(\text{C}^+) = 1.6 \times 10^{19} \text{ cm}^{-2}$ . For the foreground cloud in NGC 2024 these authors estimated  $N(\text{C}^+) \geq 10^{18} \text{ cm}^{-2}$  for a gas temperature above 40 K, but this is a very extreme region. The  $N(\text{C}^+)$  we obtain for the foreground and background clouds in the S 1 PDR are about 50% of the column densities estimated for NGC 2024 and the temperatures we estimate are also much lower. Using the stellar parameters for S 1 Larsson & Liseau (2017) estimated the FUV flux in the PDR to be  $5000 G_0$ . In another method we first estimated the total far-infrared (FIR) intensity from the PACS 70 and  $160 \mu\text{m}$  flux densities (Fig A.1) following the method described by Roccatagliata et al. (2013). Next we assumed that the FUV energy absorbed by the grains is re-radiated in the far-infrared (Mookerjea et al. 2011) and estimated the FUV flux,  $I_{\text{FUV}}$  ( $6 \text{ eV} < h\nu < 13.6 \text{ eV}$ ) impinging onto the cloud surfaces from the emergent FIR intensities ( $I_{\text{FIR}}$ ) using  $I_{\text{FUV}}$  (expressed in units of  $G_0$ ) =  $4\pi \frac{I_{\text{FIR}}}{G_0}$ . From the second approach, we find the FUV intensity at the position  $\Delta\alpha = +65''$ ,  $\Delta\delta = +58''$  to be  $3100 G_0$ . The [OI(145)]/[OI(63)] ratio at this position is 0.15, which is much larger than the typical ratio of 0.05–0.1 found in PDRs when both lines are optically thin. Larsson & Liseau (2017) explained the high values of [OI(145)]/[OI(63)] ratio to be due to [O I](63) being partially absorbed by a cold fore-

ground cloud, while [O I](145) remained unaffected. Our observations support this conjecture. The OI(145) emission, however, should mostly be optically thin. We can therefore use the [O I](145)/[C II] ratio and compare it to predictions of the plane-parallel PDR model by Kaufman et al. (2006). At this position the [O I](145)/[C II] ratio is 0.27 (in energy units), which for the FUV intensities of 3000 and 5000 G<sub>0</sub> correspond to the densities of  $4 \times 10^3 \text{ cm}^{-3}$  and  $3 \times 10^3 \text{ cm}^{-3}$  respectively. This matches very well with the critical density of the 158  $\mu\text{m}$  transition of [C II]. The critical density of the [O I] 145  $\mu\text{m}$  transition however is  $> 10^6 \text{ cm}^{-3}$ , suggesting that [O I] mostly comes from high density gas compressed between the [C II] emitting gas and the surrounding dense molecular cloud. For the above mentioned results the plane-parallel PDR model predicts an integrated intensity of  $100 \text{ K km s}^{-1}$  for the [C II] line. The background component for the two-component LTE model fitted to the observed spectrum corresponds to an integrated intensity of  $170 \text{ K km s}^{-1}$ . This suggests the existence of multiple [C II] emitting PDR surfaces in contrast to a single PDR slab, and is consistent with the scenario in which high density clumps with PDR surfaces emitting both [C II] and [O I](145) and low density PDR gas emitting only [C II] co-exist.

In this analysis, we have assumed that the entire [C II] emission arises from neutral PDR. However since carbon has an ionization potential of 11.26 eV, C<sup>+</sup> is also likely to exist in the H II region, and this will contribute to some extent to the observed [C II] emission. As detailed in Sec. 3, based on radio observations the emission from the H II region is rather faint, 4 mJy at 5 GHz. The diameter of the H II region  $< 20''$ , which is more than three times smaller than the strongest emission feature observed in [C II] and the other PDR tracers. These indicate that the contribution of the H II region to the [C II] emission is likely to be insignificant, although an accurate estimate of  $n_e$  not being available direct comparison with the models by Abel (2006) is not possible. An alternative method, is to compare with the fine-structure transitions of N<sup>+</sup> at 122 and 205  $\mu\text{m}$ , since these lines arise only in the H II region and have excitation condition and critical density similar to that of [C II]. For this purpose we have used the GREAT/SOFIA observations of the 205  $\mu\text{m}$  [N II] spectra. We do not have any detection of the 205  $\mu\text{m}$  line in the entire observed region good to an r.m.s. of integrated intensity of  $0.7 \text{ K km s}^{-1}$ . Abel (2006) showed that the [C II] intensities originating from H II regions and the intensities of the [N II] 205  $\mu\text{m}$  line are tightly correlated following the relation  $\log I_{\text{H}^+}^{\text{CII}} = 0.937 \log I_{\text{H}^+}^{\text{NII}} + 0.689$  ( $\text{erg cm}^{-2} \text{ s}^{-1}$ ). Considering the [N II] (205  $\mu\text{m}$ ) beamsize of  $21''$ , for the upper limit of [N II] intensity being  $0.7 \text{ K km s}^{-1}$ , we obtain  $I_{\text{H}^+}^{\text{CII}} \sim 22 \text{ K km s}^{-1}$ . The peak integrated intensity of the observed [C II] map is  $183 \text{ K km s}^{-1}$  and goes down to about  $130 \text{ km s}^{-1}$  in a radius of  $20''$  (upper limit on the size of the H II region) from the peak position. Thus we derive an upper limit of 12-17% for the contribution of the H II region to the [C II] emission. Given that the contribution is low and is also an upper limit, we conclude that our assumption that the entire [C II] arises from the neutral PDR does not affect the outcome of PDR models.

## 7. Summary & Conclusion

We have used the velocity information of the [C II] data observed with SOFIA/GREAT to obtain a cohesive picture of the geometry and illumination of the PDR around S 1 in  $\rho$  Ophiuchus. The [C II] emission appears to arise from both photo-evaporated flow from the dense PDR shell as well as from ionized gas inside the PDR shell. The [C II] emitting PDR is of moderate density

( $\sim 10^3 \text{ cm}^{-3}$ ), while the 63 and 145  $\mu\text{m}$  emission of [O I] requires much higher densities, i.e., it is mostly coming from the compressed neutral layer between the ionized C<sup>+</sup> gas and the dense surrounding cloud as well as from dense clumps embedded in the diffuse ionized gas. The [C II] map was observed during the Early Science phase of SOFIA and does not cover the nebula to the north-east, which prohibits us from fully constraining the geometry of the C II region excited by S 1. With the Low Frequency Array (LFA) (Risacher et al. 2016), which is a  $2 \times 7$  pixel LFA array, where each pixel is about four times as sensitive as the L2 receiver used in Early Science, one can map the whole S 1 reflection nebula with significantly higher S/N in a fraction of the time it took to obtain the [C II] map discussed here. Since the LFA array is operated in parallel with the High Frequency Array (HFA) in upGREAT, one will additionally get velocity resolved [O I] 63  $\mu\text{m}$  the same time. The only thing missing to fully characterize the PDR emitting regions is high-J CO lines, which will be quite strong in the PDR shell. We know from our work on NGC 2023 (Sandell et al. 2015) that the hot molecular gas in the PDR starts to dominate from  $J = 6-5$  upwards. CO(6-5), (7-6), and (8-7) can be observed with ground based telescopes, while upGREAT on SOFIA can observe higher J transitions starting from CO(11-10). To accurately determine the density and temperature of the hot molecular PDR emission we therefore need follow up observations of high-J CO transitions both with ground based telescopes and SOFIA.

*Acknowledgements.* Based on observations made with the NASA/DLR Stratospheric Observatory for Infrared Astronomy (SOFIA). SOFIA is jointly operated by the Universities Space Research Association, Inc. (USRA), under NASA contract NAS2-97001, and the Deutsches SOFIA Institut (DSI) under DLR contract 50 OK 0901 to the University of Stuttgart. The development of GREAT was financed by the participating institutes, by the Federal Ministry of Economics and Technology via the German Space Agency (DLR) under Grants 50 OK 1102, 50 OK 1103 and 50 OK 1104 and within the Collaborative Research Centre 956, sub-projects D2 and D3, funded by the Deutsche Forschungsgemeinschaft (DFG). This research has made use of the VizieR catalogue access tool, CDS, Strasbourg, France. The original description of the VizieR service was published in A&AS 143, 23.

## References

- Abel, N. P. 2006, MNRAS, 368, 1949
- Andersson, B.-G., & Potter, S. B. 2007, ApJ, 665, 369
- André, P., Ward-Thompson, D., Barsony, M. 1993, ApJ, 406, 122
- André, P., Montmerle, T., Feigelson, E. D., et al. 1988, ApJ, 335, 940
- Böhlin, R. C., Savage, B. D., & Drake, J. F. 1978, ApJ, 224, 132
- Bouvier, J., & Appenzeller, I. 1992, A&AS, 92, 481
- Brown, R. L., & Zuckerman, B. 1975, ApJ, 202, L125
- Buckle, J. V., Hills, R. E., Smith, H., et al. 2009, MNRAS, 399, 1026
- Chini, R. 1981, A&A, 99, 346
- Cohen, M., & Kuhl, L. V. 1979, ApJS, 41, 743
- Frerking, M. A., Langer, W. D., & Wilson, R. W. 1982, ApJ, 262, 590
- Graf, U. U., Simon, R., Stutzki, J., et al. 2012, A&A, 542, L16
- Grasdalen, G. L., Strom, K. M., & Strom, S. E. 1973, ApJ, 184, L53
- Habing, H. J. 1968, Bull. Astron. Inst. Netherlands, 19, 421
- Herter, T. L., Vacca, W. D., Adams, J. D., et al. 2013, PASP, 125, 1393
- Herter, T. L., Adams, J. D., De Buizer, J. M., et al. 2012, ApJ, 749, L18
- Heyminck, S., Graf, U. U., Güsten, R., et al. 2012, A&A, 542, L1
- Hohle, M. M., Neuhäuser, R., & Schutz, B. F. 2010, Astron. Nachr., 331, 349
- Hollenbach, D. A., & Tielens, A. G. G. M. 1999 Rev. of Modern Physics, 71, 173
- Kaufman, M. J., Wolfire, M. G., & Hollenbach, D. J. 2006, ApJ, 644, 283
- Je, H., Lee, J.-E., Lee, S., et al. 2015, ApJS, 217, 6
- Lada, C. J., & Wilking, B. A. 1984, ApJ, 287, 610
- Langer, W. D., Velusamy, T., Pineda, J. L., et al. 2010, A&A, 521, L17
- Larsson, B., & Liseau, R. 2017, A&A, 608, A133
- Lee, A., Green, G. M., Schlafly, E. F., et al. 2018, ApJ, 854, 79
- Liseau, R., Larsson, B., Luntilla, T., et al. 2015, A&A, 578, A131
- Loren, R. B., 1989, ApJ, 338, 902
- Loren, R. B., Wootten, A., & Wilking, B. A. 1990, ApJ, 365, 269

- Lorente, B. 2006 "VO compliant CAM products" memo at <https://www.cosmos.esa.int/web/iso/guide-to-iso-data-products>
- Montmerle, T., Koch-Miramont, L., Falgarone, E., et al. 1983, ApJ, 269, 182
- Mookerjea, B., Kramer, C., Buchbender, C., et al. 2011, A&A, 586, A37
- Mookerjea, B., Israel, F., Kramer, C., et al. 2016, A&A, 532, A152
- Motte, F., André, P., & Neri, R. 1998, A&A, 336, 150
- Nisini, B., Santangelo, G., Giannini, T., et al. 2015, ApJ, 801, 121
- Ortiz-León, G. N., Loinard, L., Kounkel, M. A., et al. 2017, ApJ, 834, 141
- Ossenkopf, V., Röllig, M., Neufeld, D. A., et al. 2013, A&A, 550, A57
- Padgett, D. L., Rebull, L. M., Stapelfeldt, K. R., et al. 2008, ApJ, 672, 1013
- Palmeirim, P., André, P., Kirk, J., et al. 2013, A&A, 550, A38
- Richichi, A., Leinert, Ch., Jameson, R., & Zinnecker, H. 1994, A&A, 287, 145
- Rieke, G. H., Rieke, M. J., & Paul, A. E. 1989, ApJ, 336, 752
- Rieke, G. H., & Lebofsky, M. J. 1985, ApJ, 288, 618
- Risacher, C., Güsten, R., & Stutzki, J., et al. 2016, A&A, 595, A34
- Roccatagliata, V., Preibisch, T., Ratzka, T., & Gaczkowski, B. 2013, A&A, 554, A6
- Sandell, G., Mookerjea, B., Güsten, R., et al. 2015, A&A, 578, A41
- Shirley, Y. L. 2015 PASP, 127, 299
- Simon, M., Ghez, A. M., Leinert, Ch., et al. 1995, ApJ, 443, 625
- Schmidt-Kaler, Th. 1982, *Landolt-Bornstein New Series*, Vol. 2b, Springer Verlag, New York
- Tielens, A. G. G. M., & Hollenbach, D. 1985, ApJ, 291, 722
- Vastel, C., Bottinelli, S., Caux, E., Glorian, J.-M., & Boiziot, M. 2015, SF2A-2015: Proceedings of the Annual meeting of the French Society of Astronomy and Astrophysics, 313
- Vuong, M. H., Montmerle, T., Grosso, N., et al. 2003, A&A, 408, 581
- Weintraub, D. A., Kastner, J. H., Griffith, L. L., et al. 1993, AJ, 105, 271
- White, G. J., Drabek-Maunder, E., Rosolowsky, E., et al. 2015, MNRAS, 447, 1996
- Wilking, B. A., Cagné, M., & Allen, L. E. 2008, in *Handbook of Star Forming Regions*, Vol. 2, ed. B. Reipurth (San Francisco, CA ASP), 351
- Wilking, B. A., Meyer, M. R., Robinson, J. G., et al. 2005, AJ, 130, 1733
- Wilson, T. L., & Rood, R. 1994, ARA&A, 32, 191
- Young, E. T., Becklin, E. E., Marcum, P. M., et al. 2012, ApJ, 749, L17
- Yui, Y. Y., Nakagawa, T., Doi, Y., et al. 1993, ApJ, 419, L37

### Appendix A: PACS continuum images and derived FUV intensity map

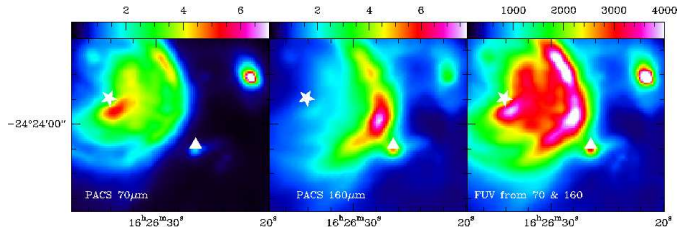


**Fig. A.1.** PACS continuum maps at 70 (left) and 160 (middle)  $\mu\text{m}$ , both at the resolution of the 160  $\mu\text{m}$  map. (Right) FUV intensity derived from the total FIR intensity calculated from the PACS 70 and 160  $\mu\text{m}$  continuum intensities using the method described in text.

### Appendix B: Channel Maps for Molecular Tracers

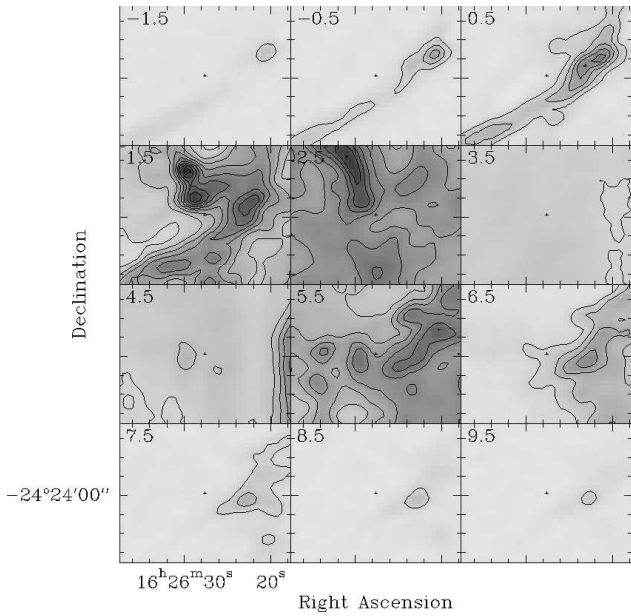


**Fig. B.1.** CO(3–2) channel maps of 1 km s<sup>−1</sup> wide velocity channels spaced by 1 km s<sup>−1</sup>.

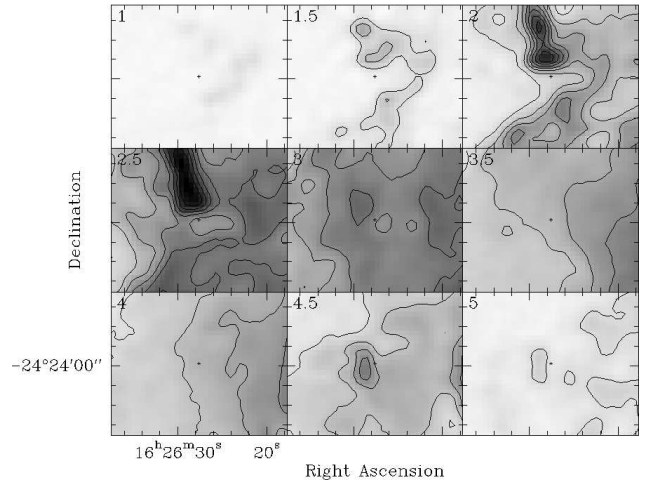


**Fig. B.2.** <sup>13</sup>CO(3–2) channel maps of 1 km s<sup>−1</sup> wide velocity channels spaced by 1 km s<sup>−1</sup>.

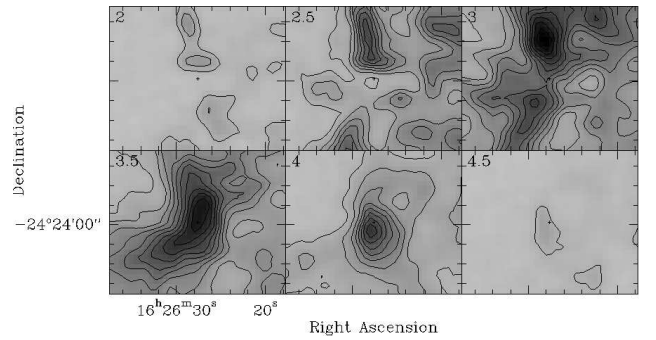


**Fig. B.3.** C<sup>18</sup>O(3–2) channel maps of 1 km s<sup>−1</sup> wide velocity channels spaced by 1 km s<sup>−1</sup>.

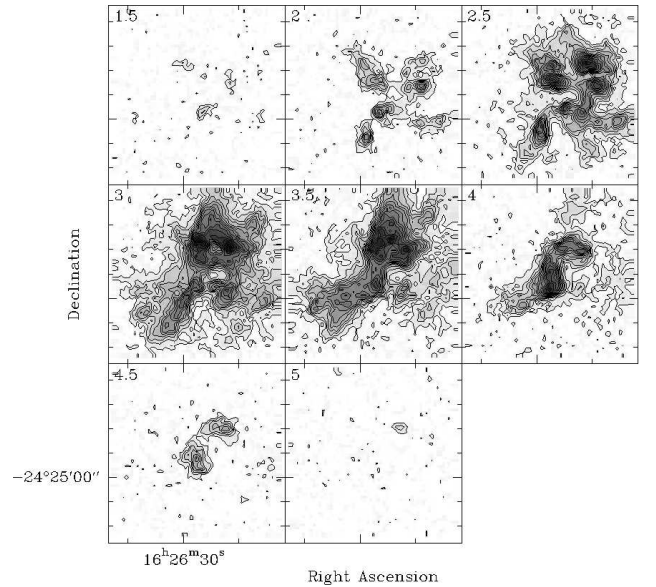


**Fig. B.4.** HCO<sup>+</sup>(4–3) channel maps of 0.5 km s<sup>−1</sup> wide velocity channels spaced by 0.5 km s<sup>−1</sup>.